Carbon 219 (2024) 118764

Contents lists available at ScienceDirect

Carbon

journal homepage: www.elsevier.com/locate/carbon

Oxidation dynamics of soot or carbon black accounting for its core-shell structure and pore network

Georgios A. Kelesidis [a,b], Patrizia Crepaldi [a], Sotiris E. Pratsinis [a,*]

[a] Particle Technology Laboratory, Institute of Process Engineering, Department of Mechanical and Process Engineering, ETH Zürich, Sonneggstrasse 3, CH-8092, Zürich, Switzerland

[b] Nanoscience and Advanced Materials Center (NAMC), Environmental and Occupational Health Science Institute, School of Public Health, Rutgers, The State University of New Jersey, 170 Frelinghuysen Road, Piscataway, NJ, 08854, USA

ARTICLE INFO

Keywords:
Carbon black
Soot
Oxidation
Porosity
Surface area

ABSTRACT

Internal oxidation is most important for removal of soot in diesel particulate filters. Furthermore, it enhances the porosity of carbon blacks (CBs), increases their specific surface area, *SSA*, determining their performance in batteries, inks and tires, as well as their environmental and health impact. Current models for oxidation of soot or CB neglect its fractal-like pore network during internal oxidation and underestimate its *SSA* by 60 % on average! Here, a lattice Monte Carlo (LMC) model elucidates both external and internal oxidation dynamics of soot (or CB) accounting for its fractal-like pore structure, for the first time to the best of our knowledge. Random internal oxidation takes place at the bulk soot (or CB), expanding its pore network and increasing the pore fractal dimension, D_{fp}, up to 3, in good agreement with data. This increases the *SSA* up to a factor of ten at 75 % conversion. In the presence of a less reactive shell though, internal oxidation stops after the reactive core is consumed. Thus the *SSA* levels off at large conversions (>50 %). Hence, accounting for the realistic core-shell, fractal-like pore structure during simultaneous external and internal oxidation nicely explains several measurements of soot and CB D_{fp}, *SSA* and particle diameter. So the LMC-derived oxidation dynamics of soot or CB presented here can be used to assist the design of highly porous CB grades from first principles, as well as the mitigation of soot emissions by enhancing their oxidation.

1. Introduction

Oxidation facilitates the elimination of soot emissions to minimize their environmental and health footprint. For example, soot nanoparticles are partially oxidized in regenerative traps and particulate filters at the engine exhaust during diesel [1] and jet fuel [2] combustion. This increases their porosity and specific surface area, *SSA* [1], and thus their toxicity [3] and propensity to act as cloud condensation nuclei [4]. Furthermore, internal oxidation enhances the porosity of carbon blacks and determines their performance in various applications (e.g. tires, inks, paints). Low temperature oxidation has been used to optimize the porosity of carbon blacks [5] and candle soot [6] and improve their performance in electrochemical storage. So, a quantitative understanding of the carbonaceous nanoparticle (CNP) porosity dynamics during oxidation is essential for the process design of highly porous carbon black grades [7], as well as for the mitigation of the impact of soot on public health and climate [8].

The internal porosity of CNPs depends on the combustion conditions during the CNP formation and growth [9]. For example, nascent soot formed at low temperatures and short residence times is rather amorphous and contains mostly single and randomly arranged PAHs [10]. In contrast, mature soot [10] and carbon black [11] particles formed at high temperatures and long residence times consist of a graphitic, less reactive porous shell of stacked and concentrically-oriented PAHs [12] that encloses an amorphous, reactive core [13]. The average PAH length of nascent and mature soot or carbon black varies with fuel type (e.g. benzene vs. ethanol [14]). Both nascent and mature CNPs contain micropores having width that ranges from 0.2 [15] to 0.9 nm [16] between each PAH stack. Small angle X-ray scattering [17], Ar, CO_2 [18] and N_2 adsorption [19] revealed that the pores of soot and carbon blacks form fractal-like networks having a fractal dimension, D_{fp}, of about 2–2.5. In the absence of oxidation, the total pore surface area of CNPs is negligible compared to their external particle surface area [20]. So, the specific surface area, *SSA*, of unoxidized CNPs ranges from 50 m^2/g for diesel

* Corresponding author.
E-mail address: sotiris.pratsinis@ptl.mavt.ethz.ch (S.E. Pratsinis).

https://doi.org/10.1016/j.carbon.2023.118764
Received 30 October 2023; Received in revised form 22 December 2023; Accepted 22 December 2023
Available online 23 December 2023

Table 1
Initial $D_{fp,o}$ of pore networks created here by DLA for unoxidized CNPs, along with those obtained in literature using DLA [44,45] and experimental data from acetylene black [18], Printex 95 [19], NIST and NEU soot [17].

	Experimental data				DLA simulations		
	Acetylene black [18]	Printex 95 [19]	NIST [17]	NEU [17]	Eggerdorfer & Pratsinis [44]	Tolman & Meakin [45]	This work
Pore fractal dimension, $D_{fp,o}$	2	2.42	2.37	2.19	2.25	2.49	2.21 ± 0.08

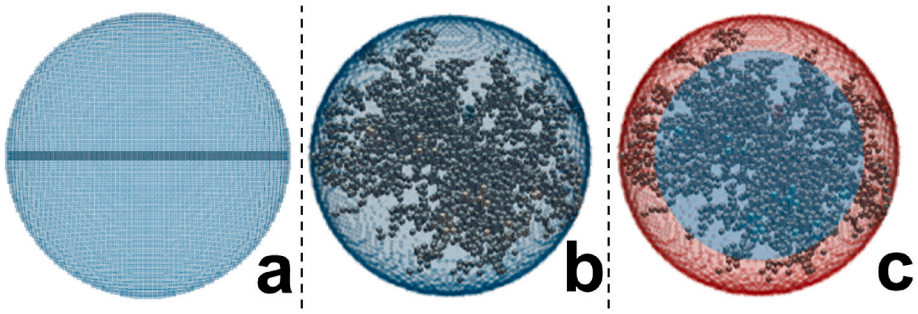

Fig. 1. Representative carbonaceous nanoparticles (CNPs) containing a single straight pore (a), or a fractal-like pore network without (b) and with (c) a surrounding shell (red-shaded). The dark blue cubic cells represent the pores. The light blue cells in (b) and (c) represent reactive solid sites, while the red-shaded ones in (c) represent non-reactive solid sites of the particle shell.

soot [20] to 300 m^2/g for fine carbon black grades [21].

The evolution of CNP porosity during oxidation at various temperatures, *T*, has been elucidated experimentally for NEU, NIST [17], diesel soot [20] and carbon blacks (e.g. Regal 600 [22] and Printex 95 [19]). That way, it was shown that O_2 reacts at the external surface of carbon black particles at 800 °C, reducing their diameter without affecting their internal structure [19]. So, external oxidation enhances the CNP *SSA* only up to 50 % at a 75 % conversion [19]. At low temperatures (e.g. 500–600 °C), O_2 diffuses and reacts within the bulk CNP [23]. Internal oxidation compacts the pore network of soot [17] and carbon black [19], increasing its D_{fp} up to 2.9. This results in hollow carbon black [19], diesel [20] and biodiesel [24] soot particles and increases their *SSA* up to a factor of four at 50–75 % conversion [20]. In this regard, the detailed experimental characterization of the CNP porosity obtained at various *T* can enable the derivation of robust models for the external and internal oxidation of CNPs.

External oxidation of CNPs is typically simulated using moment [25], fixed [26] and moving monodisperse [27] or polydisperse [23] sectional models by reducing uniformly the primary particle diameter, d_p, following closely the analytical shrinking particle model [28]. Fixed [29] and moving [23] sectional models have been used also to derive the internal oxidation dynamics of CNPs containing cylindrical pores. These pores grow uniformly by internal oxidation at low temperatures [23]. Despite this simplification, a moving sectional model for external and internal oxidation [23] explained mobility size distribution data from nascent [30] and mature soot [31] oxidized at high and low *T*. However, the *SSA* derived by this model is up to 60 % smaller than that measured at 60 % conversion [22]. So, accounting for the realistic fractal-like pore network of CNPs seems to be essential to describe their porosity and *SSA* dynamics.

In this regard, lattice Monte Carlo (LMC) models [32] have been used to elucidate the uniform [33] or random [34] internal oxidation of single [35] and multi-component [36] coal particles, as well as the reduction of iron oxide particles [37] accounting for their fractal-like pore network [38]. Here, a LMC model is developed to simulate the concurrent external and internal oxidation of CNPs, for the first time to the best of our knowledge. Uniform and random internal oxidation of CNPs containing a single cylindrical pore are firstly derived by LMC and compared to the shrinking particle model for external oxidation [28]. Then, the simultaneous external and internal oxidation of CNPs containing fractal-like pore networks is elucidated at high and low temperatures, respectively. The LMC-derived evolution of D_{fp} and *SSA* is validated over a wide range of experimental data from NEU, NIST [17], diesel soot [20] and commercial carbon blacks [19,22]. The impact of the CNP core-shell structure on the oxidation dynamics is also quantified.

2. Methods

2.1. Internal structure of CNPs

Spherical CNPs with diameter, d_p = 18 nm are discretized into a cubic lattice of 113′100 cells. The CNP d_p used here is on par with the carbon black [19] and soot [31] d_p used often in oxidation experiments. Each cell *i* can be part of the CNP solid or pore networks having a solid mass fraction, $y_i = 1$ or 0, respectively. The cell size is set to 0.3 nm that is on par with the smallest pore sizes of 0.2 and 0.36 nm used in sectional models [23] and molecular dynamics [39], respectively. The oxidation dynamics of CNPs having a single straight pore of 18 nm length and 0.6 nm width are simulated. The initial fractal dimension, $D_{fp,o} = 1$ derived here for this pore using the Sandbox algorithm [40] is in excellent agreement with the theoretical $D_{fp} = 1$ for linear structures [41].

CNPs containing fractal-like pore networks are also created here using a diffusion limited aggregation (DLA) algorithm [42]. DLA results in percolated pore networks, similar to those of large coal [32–36] and iron oxide [37] particles obtained from percolation theory [43]. In brief, a single pore cell is placed at the CNP center. Then, new pore cells are generated next to existing ones based on diffusion-limited random walks [42], resulting in a CNP porosity of 2 % [23] and matching that way the SSA_o of 240.3 m^2/g measured for unoxidized carbon black [19]. The $D_{fp,o}$ = 2.21 ± 0.08 of the fractal-like pore networks derived that way (Table 1) is in excellent agreement with that obtained by Eggersdorfer & Pratsinis [44] for DLA-derived structures with similar size, but slightly smaller than that of Tolman & Meakin [45] obtained for larger

fractal-like networks. This can be attributed to finite size effects [46]. The $D_{fp,o}$ derived here is well within the range of the $D_{fp,o}$ measured for unoxidized carbon blacks (2–2.42) [18,19] and soot (2.19–2.37) [17]. That way realistic initial CNP pore structures are used here before oxidation starts. The $D_{fp,o}$ derived here is also on par with the $D_{fp,o} = 2.53$ obtained for large coal [32–36] and iron oxide [37] particles from percolation theory [43].

CNPs having a core-shell structure are also generated to investigate the limited shell reactivity of mature soot [47] and carbon black [48] nanoparticles. The CNP shell reacts much more slowly with O_2 due to its large degree of graphitization [12]. The diameter of the reactive core, d_c, is varied from $0.5d_p$ to $0.75d_p$. This range is consistent with the $d_c = 0.4d_p$ - $0.8d_p$ obtained from microscopy images of mature soot from diesel engines [12] and diffusion flames [49]. CNPs with $d_c/d_p = 0$ are also simulated here to account for graphitic CNPs (e.g. Fischer-Tropsch soot [24]) that undergo mostly external oxidation even at low T. Fig. 1 summarizes the pore structures used in this work.

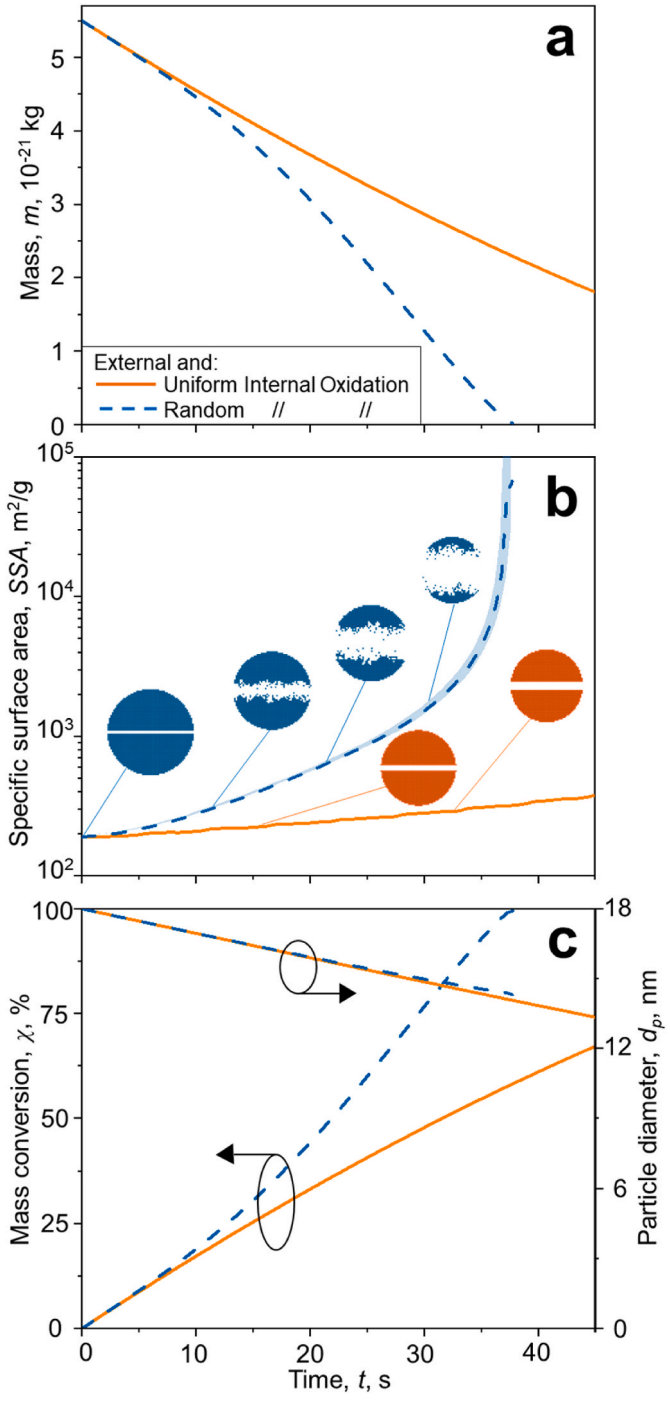

Fig. 2. LMC-derived evolution of m (a), SSA (b), χ (c: left ordinate) and d_p (c: right ordinate) as a function of t during simultaneous external and uniform (solid lines, orange insets) or random (broken lines, blue insets) internal oxidation of CNPs containing a single straight pore at 550 °C.

2.2. Lattice Monte Carlo simulation of CNP oxidation

Lattice Monte Carlo (LMC) is a computational algorithm that relies on random sampling to simulate stochastic processes (e.g. diffusion and reaction of gases in porous materials) on a cubic lattice [32]. Here, LMC is used to elucidate the oxidation dynamics of CNPs at 550 or 800 °C and 10 vol % of O_2 [19]. The evolution of CNP mass, m, as a function of time, t, during external and internal oxidation is [23]:

$$\frac{dm}{dt} = -\omega\,(A_{ext} + A_{int}) \tag{1}$$

where $\omega = 9.5{\cdot}10^{-8}$ and $1.2{\cdot}10^{-5}$ kg/(m^{2}s) are the oxidation rates of Nagle & Strickland-Constable (NSC) at 550 and 800 °C, respectively [50], while A_{ext} and A_{int} are the external and internal areas, respectively. So, ω is the same for both external and internal oxidation, consistent with "overall" rates derived for external and internal oxidation of diesel [51] and flame [52] soot.

At $T = 800$ °C, internal oxidation is negligible [19] and integrating Eq. (1) yields:

$$\Delta m_{ext} = -\omega A_{ext}\Delta t \tag{2}$$

where Δm_{ext} is the mass removed by external oxidation after time Δt. The CNP m at t is:

$$m(t) = \rho\,\frac{\pi}{6} d_p(t)^3 \tag{3}$$

where $\rho = 1.8$ g/cm^3 is the CNP bulk density [53]. The d_p at $t + \Delta t$ can be obtained by combining Eqs. (2) and (3):

$$d_p(t+\Delta t)^3 = d_p(t)^3 - \frac{6\omega A_{ext}\Delta t}{\pi\rho} \tag{4}$$

So, solid cells with center of mass larger than $d_p(t + \Delta t)$ are converted to CO_2 by external oxidation and their y_i is set to zero.

At $T = 550$ °C, the Thiele effectiveness factor is about 1 [23] and O_2 molecules can diffuse throughout the small CNPs investigated here [15]. The total mass, Δm_{int}, removed by internal oxidation at Δt is obtained by integrating Eq. (1):

$$\Delta m_{int} = -\omega A_{int}\Delta t \tag{5}$$

Based on the uniform internal oxidation model [33], all internal solid cells adjacent to pores are oxidized uniformly resulting in:

$$\Delta m_{c,i} = -\omega A_{c,i}\Delta t \tag{6}$$

where $\Delta m_{c,i} = m_{c,i}(t + \Delta t) - m_{c,i}(t)$ is the mass of cell i removed by internal oxidation and $A_{c,i}$ is its external area. At small t, uniform internal oxidation is incomplete and solid cells are only partly converted to CO_2. So, y_i is given by:

$$y_i(t) = \frac{m_{c,i}(t)}{m_{c,o}} \tag{7}$$

where $m_{c,o}$ is the initial cell mass before any internal oxidation takes place. The cell y_i at $t + \Delta t$ is obtained by combining Eqs. (6) and (7):

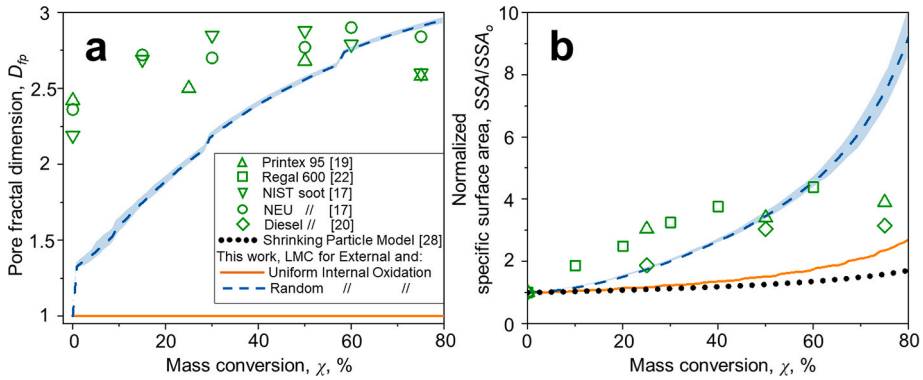

Fig. 3. LMC-derived D_{fp} (a) and normalized SSA/SSA_o (b) as a function of χ during concurrent external and uniform (solid lines) or random (broken lines) internal oxidation of CNPs containing a single straight pore, along with the shrinking particle model (dotted line [28]) and experimental data from Printex 95 (triangles [19]) and Regal 600 (squares [22]) carbon blacks, as well as NIST (inverse triangles [17]), NEU (circles [17]) and diesel (diamonds [20]) soot.and have $D_{fp} > 1$ [17–19].

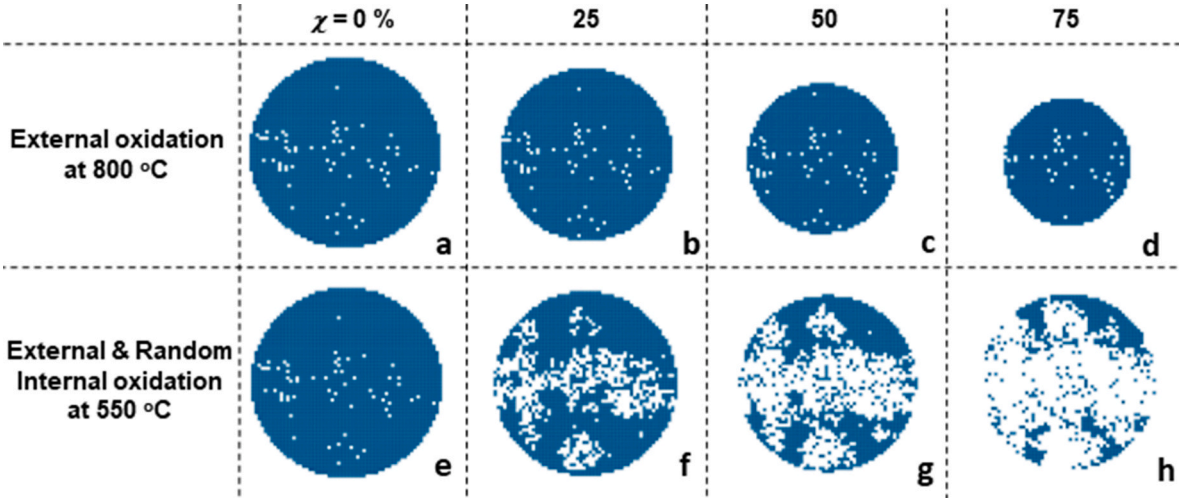

Fig. 4. Cross-sections of CNPs containing fractal-like pore networks with initial $D_{fp} = 2.21 \pm 0.08$ (Table 1) derived by LMC during solely external (a–d) and concurrent external and random internal (e–h) oxidation at 800 (a–d) or 550 °C (e–h) and $\chi = 0$, 25, 50 and 75 %.

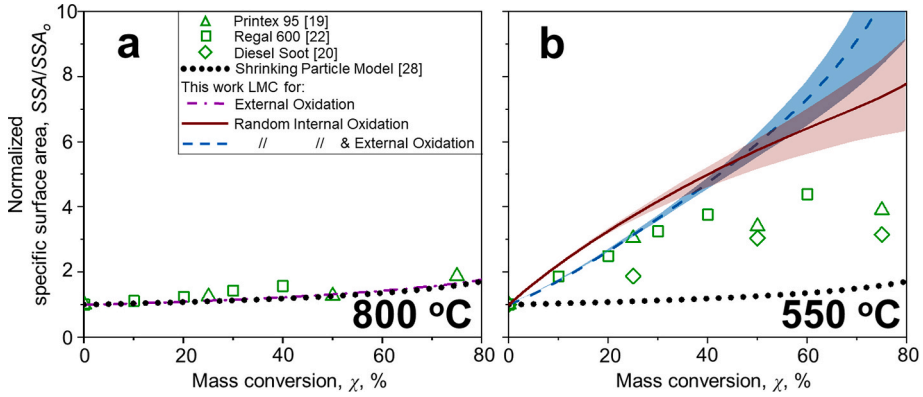

Fig. 5. LMC-derived SSA/SSA_o as a function of χ during solely external (a) and concurrent external & random internal oxidation (b) at 800 (a: dot-broken line) or 550 °C (b: broken line) of CNPs containing fractal-like pore networks, along with the shrinking particle model (dotted lines [28]) and experimental data from Fig. 3.

$$y_i(t+\Delta t) = y_i(t) - \frac{\omega\, A_{c,i}\Delta t}{m_{c,o}} \tag{8}$$

When internal oxidation is completed and $y_i = 0$, the solid cell is converted to a pore [33]. The CO_2 generated by internal oxidation is removed rapidly from the bulk CNP [33]. This is a common assumption in LMC models of coal combustion [33,34].

A random internal oxidation model [34] is also explored here to account for the random walk of O_2 in the bulk CNP [15]. So, internal solid cells adjacent to pores are selected using a random number generator [54] and oxidized completely [34]. The total number of cells, n_c, oxidized that way is given by:

$$n_c = \frac{\Delta m_{int}}{m_{c,o}} \tag{9}$$

where Δm_{int} is given by Eq. (5).

3. Results & discussion

3.1. Oxidation dynamics of CNPs containing a single straight pore

Fig. 2 shows the CNP mass, m (a), specific surface area, SSA (b), conversion, χ (c: left ordinate), and diameter, d_p (c: right ordinate), as a function of time, t, during simultaneous external and uniform (solid lines, orange insets) or random (broken lines, blue insets) internal oxidation of CNPs containing a single straight pore derived by lattice Monte Carlo (LMC) at 550 °C. The shaded area represents the statistical variation of 50 LMC simulations for external and random internal oxidation. Uniform internal oxidation results in uniform oxidation of all solid sites adjacent to pores [33]. Random oxidation results in random (stochastic) removal of solid sites adjacent to pores [34]. During concurrent external and uniform internal oxidation, the pore width increases uniformly as a function of t. This results in a linear increase of the CNP SSA and reduction of its m. This is consistent with moving sectional modeling of concurrent external and uniform internal oxidation of soot containing cylindrical pores [23]. In contrast, random internal oxidation results in a fractal-like pore network, as nicely shown by the insets in Fig. 2b. This drastically increases the porosity of CNP, enhancing its SSA and reducing its m (Fig. 2a). The evolution of d_p (Fig. 2c) is determined only by external oxidation and is not affected by internal oxidation.

Fig. 3 shows the LMC-derived pore fractal dimension, D_{fp} (a), and normalized SSA by the initial SSA_o (SSA/SSA_o) (b) as a function of χ during simultaneous external and uniform (solid lines, orange insets) or random (broken lines, blue inset) internal oxidation of CNPs containing initially a single straight pore, along with the shrinking particle model (dotted line [28]) and experimental data from Printex 95 (triangles [19]) and Regal 600 (squares [22]) carbon blacks, as well as NIST (inverse triangles [17]), NEU (circles [17]) and diesel (diamonds [20]) soot. The shaded areas represent the statistical variation of the LMC simulations. The soot (inverse triangles, circles [17], diamonds [20]) and carbon black (triangles [19], squares [22]) data have been obtained at 500 and 550 °C, respectively. Their SSA_o has been measured by N_2 adsorption [19] or microscopy [20,22], while their SSA evolution has been obtained by N_2 adsorption. Uniform internal oxidation does not alter the pore morphology. So, $D_{fp} = 1$ at all χ (Fig. 3a), while SSA doubles by $\chi = 80$ % (Fig. 3b). Thus, accounting for concurrent external and uniform internal oxidation of a single straight pore results in up to 50 % larger SSA than that obtained by the shrinking particle model for external oxidation only [28] (dotted line, Fig. 3b). However, this uniform oxidation model vastly underestimates (up to 60 %) the measured SSA of CNPs. Random internal oxidation results in fractal-like pore networks with large D_{fp} of about 3 at $\chi = 80$ %. This increases rapidly the SSA, explaining some of the large SSA measured at $\chi > 50$ %. However, this model for simultaneous external and random internal oxidation of CNPs with a single straight pore underestimates up to 50 % the SSA measured at $\chi < 50$ %. This can be attributed to the compact pore networks that make up unoxidized CNPs.

3.2. Oxidation dynamics of CNPs containing fractal-like pore networks

Fig. 4 shows cross-sections of CNPs containing fractal-like pore networks with initial $D_{fp} = 2.21 \pm 0.08$ (Table 1) derived by LMC during solely external (a-d) and concurrent external and random internal (e-h) oxidation at 800 (a-d) or 550 °C (e-h) and conversion $\chi = 0$, 25, 50 and 75 %. At 800 °C (a-d), oxidation takes place largely at the external surface of CNPs [19], reducing their diameter without much affecting their internal porosity. The internal surface area of CNPs is larger than their external one. So, at 550 °C (e-h), internal oxidation dominates increasing the CNP porosity with increasing χ, while limited external oxidation reduces only slightly the size of the CNP.

Fig. 5 shows the LMC-derived evolution of SSA/SSA_o as a function of χ during solely external (a) and simultaneous external and random internal oxidation (b) at 800 (a: dot-broken line) or 550 °C (b: broken line) of CNPs containing fractal-like pore networks, along with the shrinking particle model (dotted lines [28]) and experimental data from Fig. 3. The shaded area represents the statistical variation of the LMC simulations obtained from 50 fractal-like pore networks. In the absence of internal oxidation (a), the LMC-derived SSA increases by up to 50 % by

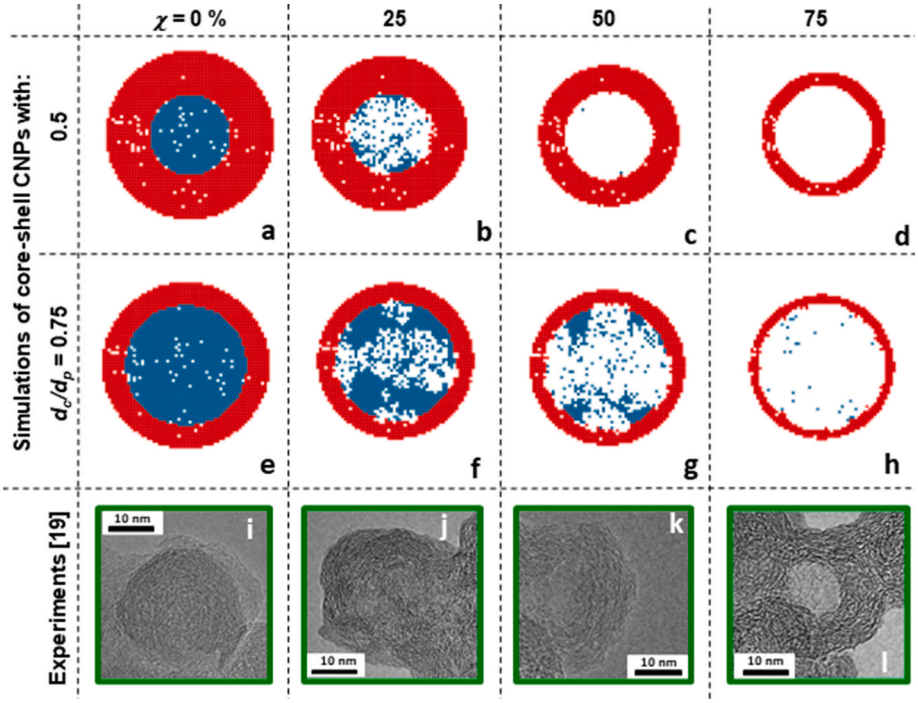

Fig. 6. Cross-sections of core-shell CNPs with $d_c = 0.5$ (a–d) or $0.75 d_p$ (e–h) derived by LMC for concurrent external and random internal oxidation at 550 °C and $\chi =$ 0, 25, 50 and 75 %, along with microscopy images of Printex 95 [19] oxidized at the same conditions (i–l).

external oxidation at 800 °C, in excellent agreement with the shrinking particle model and the data obtained at the same conditions. This further validates the present LMC simulations.

Concurrent external and random internal oxidation of CNPs containing fractal-like pore networks at 550 °C (b) increases the *SSA* by up to an order of magnitude at $\chi = 70$ %. The *SSA* evolution derived by LMC at these conditions is in good agreement with data at $\chi < 50$ %, but overestimates the measured *SSA* by 130 % on average at $\chi = 50$–80 %. This indicates that random internal oxidation levels off at such large χ for the mature soot [17,20] and carbon black [19,22] nanoparticles shown in Fig. 5, proving that their further oxidation is somehow hindered. Internal oxidation results in 20 % larger *SSA* (on average) compared to that obtained by concurrent internal and external oxidation at $\chi < 50$ % and 10 % smaller *SSA* (on average) at $\chi \geq 50$ % (Fig. 5b). Most importantly, internal oxidation overestimates the measured *SSA* by 85 % (on average). So, the slow external burning rates proposed based on microscopy images of diesel [51,55] and flame [52] soot cannot explain the measured *SSA* dynamics of diesel soot and carbon black at low *T*.

3.3. Impact of core-shell structure on the CNP internal oxidation

Fig. 6 shows the cross-sections of core-shell CNPs with a reactive core diameter, $d_c = 0.5d_p$ (a-d) or $0.75d_p$ (e-h) derived by LMC for simultaneous external and random internal oxidation at 550 °C and conversion $\chi = 0$, 25, 50 and 75 %, along with microscopy images of Printex 95 [19] oxidized at the same conditions (i-l). The shell of CNPs contains large stacks of PAHs [49] that limit its oxidation [48]. So internal oxidation of CNPs with $d_c/d_p = 0.5$ (a-d) or 0.75 (e-h) results in hollow structures at $\chi = 0.75$ %, in good agreement with those observed for Printex 95 at similar oxidation conditions [19].

Fig. 7 shows the LMC-derived *m* (a), *SSA* (b) and d_p (c) at 550 °C as a function of *t* during simultaneous external and random internal oxidation of CNPs having $d_c/d_p = 0$ (dot-broken lines), 0.5 (dotted lines), 0.75 (solid lines) and 1 (broken lines). Again, the shaded areas represent the statistical variation of the LMC simulations obtained from 50 fractal-like pore networks as in Fig. 5b. The CNPs with $d_c/d_p = 0$ are oxidized slowly, as their core is not reactive and oxidation takes place only at their external surface decreasing their diameter, as seen in Fig. 2c. So, *m* and d_p decrease, while *SSA* increases linearly with time.

The CNPs that contain a reactive core ($d_c/d_p > 0$) are oxidized faster as both internal and external oxidation take place simultaneously, consistent with moving sectional modelling [23] and microscopy measurements [48]. In the presence of a less reactive shell though ($d_c/d_p =$ 0.5 or 0.75), internal oxidation practically stops when the reactive core has been fully consumed. This levels off the *m* and *SSA* reduction. The d_p reduction is not affected by the core-shell structure of CNPs, as it is determined by external oxidation only [23].

Fig. 8 shows the LMC-derived evolution of D_{fp} (a) and SSA/SSA_o (b) as a function of χ during simultaneous external and random internal oxidation of CNPs having $d_c/d_p = 0$ (dot-broken lines), 0.5 (dotted lines), 0.75 (solid lines) and 1 (broken lines), along with experimental data from carbon blacks [19,22] and soot [17,20]. In the absence of a reactive core ($d_c/d_p = 0$), oxidation takes place only at the external CNP surface without altering its D_{fp} and SSA/SSA_o. This underestimates the measured CNP *SSA* up to 60 %. On the other hand, neglecting the less reactive shell at the CNP surface ($d_c/d_p = 1$) results in internal oxidation throughout the particle volume. This results in a fast increase of D_{fp} and SSA/SSA_o and overestimates SSA/SSA_o up to a factor of three at $\chi = 75$ %, as discussed already in Fig. 6.

In the presence of a less reactive shell ($d_c/d_p = 0.5$ or 0.75), internal oxidation gradually stops when the reactive core has been fully consumed. So, both D_{fp} and SSA/SSA_o level off at $\chi > 50$ %. The LMC-derived evolution of CNP D_{fp} and SSA/SSA_o using $d_c/d_p = 0.5$ - 0.75 nicely explains all data presented here. This indicates that the core-shell structure of the CNPs shown in Fig. 8 (symbols) determines the dynamics of their porosity during internal oxidation.

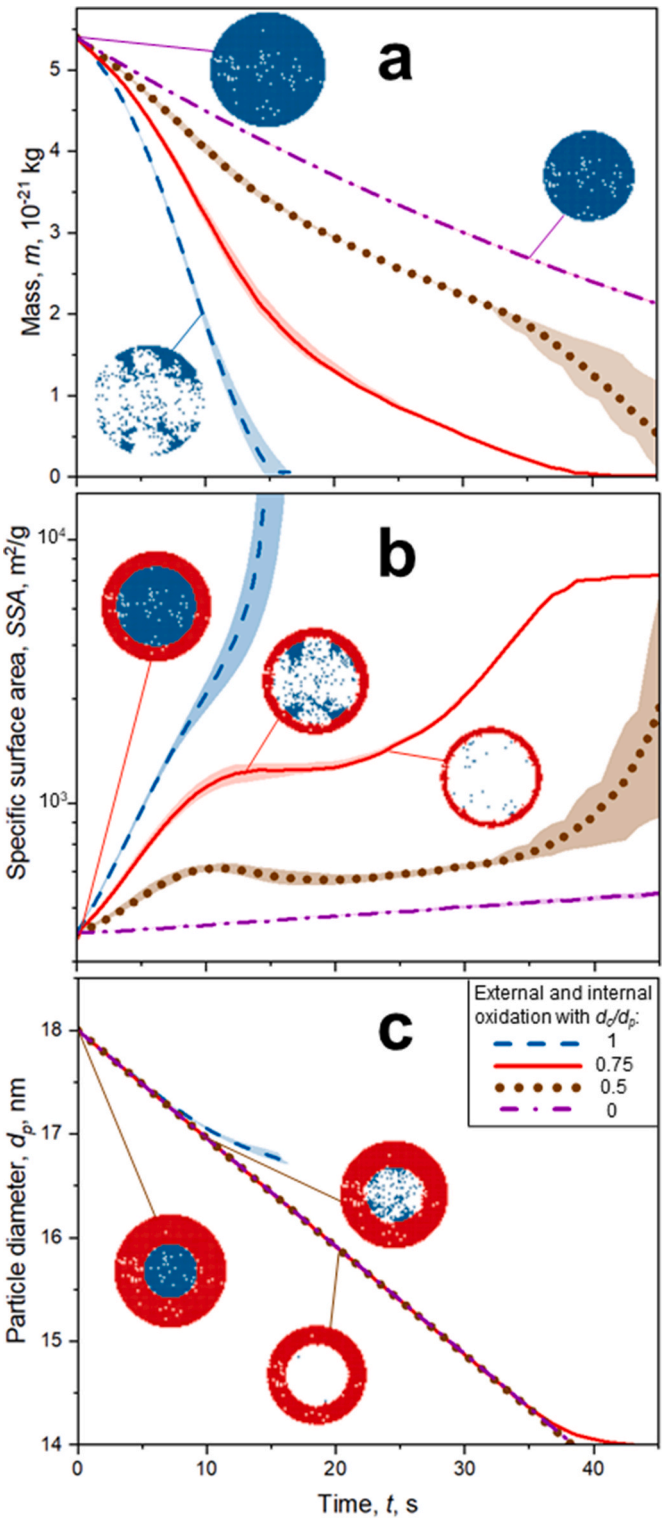

Fig. 7. LMC-derived *m* (a), *SSA* (b) and d_p (c) as a function of *t* during concurrent external and random internal oxidation of CNPs having $d_c/d_p = 0$ (dot-broken lines), 0.5 (dotted lines), 0.75 (solid lines) and 1 (broken lines).

Fig. 9 shows the normalized d_p by the initial $d_{p,o}$, $d_p/d_{p,o}$, as a function of χ derived here by LMC for external and internal oxidation of CNPs with $d_c/d_p = 1$ (broken line), 0.75 (solid line), 0.5 (dotted line) and 0 (dot-broken line) at 550 °C, along with Fischer-Tropsch (triangles [24]) and diesel soot data obtained at 500 (diamonds [20]) or 450 °C (squares, circles [51]) and exhaust gas recirculation (EGR) of

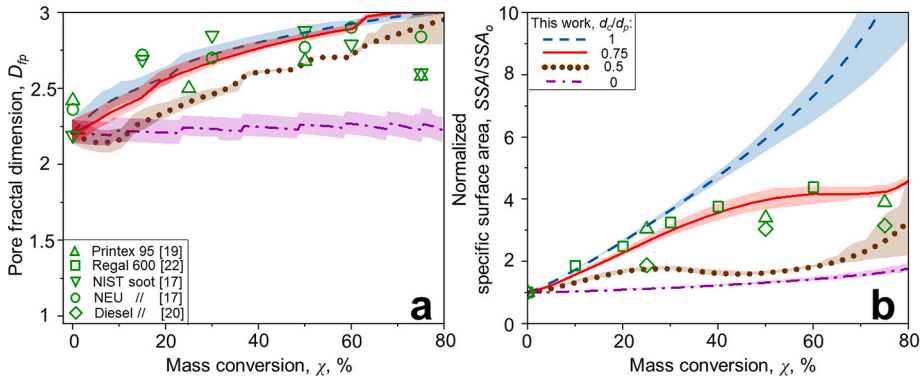

Fig. 8. LMC-derived D_{fp} (a) and SSA/SSA_o (b) as a function of χ during simultaneous external and random internal oxidation of CNPs having $d_c/d_p = 0$ (dot-broken lines), 0.5 (dotted lines), 0.75 (solid lines) and 1 (broken lines), along with experimental data from Fig. 3.

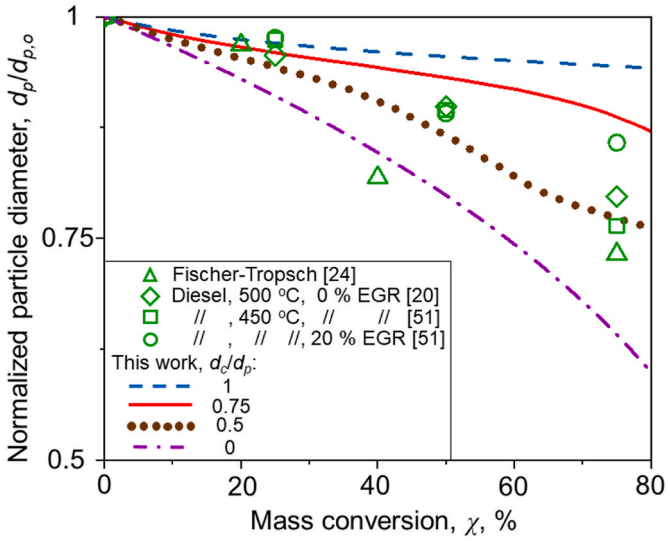

Fig. 9. Normalized d_p by the initial $d_{p,o}$ ($d_p/d_{p,o}$) as a function of χ derived here by LMC for oxidation of CNPs with $d_c/d_p = 1$ (broken line), 0.75 (solid line), 0.5 (dotted line) and 0 (dot-broken line) along with Fischer-Tropsch (triangles [24]) or diesel soot data obtained at 500 (diamonds [20]) or 450 °C (squares, circles [51]) and EGR = 0 (diamonds [20], squares [51]) or 20 % (circles [51]).

0 (diamonds [20], squares [51]) or 20 % (circles [51]). At $d_c/d_p = 0$, only external oxidation takes place and reduces d_p up to about 40 % at $\chi = 80$ %. The d_p data obtained from graphitic Fischer-Tropsch soot (triangles [24]) lie mostly between the d_p dynamics derived by LMC for d_c/d_p = 0 and 0.5. This confirms that Fischer-Tropsch soot is graphitic and undergoes mostly external oxidation. Internal oxidation is dominant at $d_c/d_p \geq 0.5$ and removes mass from the bulk CNP. So, external oxidation is limited and reduces d_p by 5–20 % at $d_c/d_p = 1$ - 0.5 and $\chi = 80$ %. In this regard, the d_p data measured for diesel soot oxidized at 450–500 °C and EGR = 0–20 % (squares, circles [51] & diamonds [20]) are in agreement with the d_p derived here by LMC for CNPs with d_c/d_p = 0.5–0.75 (solid & dotted lines). This confirms that diesel soot particles undergo both internal and external oxidation at these conditions.

4. Conclusions

Lattice Monte Carlo (LMC) simulations for concurrent external and internal oxidation were used here to elucidate the dynamics of carbonaceous nanoparticle (CNP) porosity, for the first time to the best of our knowledge. So, the evolution of the CNP specific surface area, *SSA*, during random internal oxidation is presented here for fractal-like pore networks. Internal oxidation compacts the pore network, increasing the pore fractal dimension, D_{fp}, up to 3 and enhancing the *SSA* up to an order of magnitude at 75 % conversion. In the presence of a less reactive shell though, internal oxidation stops after the more reactive core is consumed. Thus the *SSA* levels off at large conversions (>50 %) of CNPs with core-shell pore networks, in excellent agreement with experimental data for NIST, NEU [17], diesel soot [20,51] and carbon black [19,22] oxidation. In specific, most soot and carbon black data are bracketed between the LMC dynamics obtained for d_c/d_p = 0.5–0.75 (Fig. 8a). So, accounting for the realistic internal pore structure of CNPs is essential to simulate accurately their oxidation dynamics. In this regard, the present LMC model can be used to guide the design of highly porous carbon black grades by low temperature oxidation [19] and optimize their performance in various applications from first principles. The porosity dynamics obtained by LMC can be used also to derive robust oxidation rates for soot nanoparticles [23] and eliminate soot emissions by judicious air injection at the combustor exhaust [2].

CRediT authorship contribution statement

Georgios A. Kelesidis: Conceptualization, Formal analysis, Methodology, Supervision, Validation, Writing – original draft, Writing – review & editing. **Patrizia Crepaldi:** Formal analysis, Methodology, Software, Validation, Writing – original draft, Visualization. **Sotiris E. Pratsinis:** Funding acquisition, Supervision, Writing – review & editing.

Declaration of competing interest

The authors declare that they have no known competing financial interests or personal relationships that could have appeared to influence the work reported in this paper.

Acknowledgements

This research was funded by the Particle Technology Laboratory, ETH Zurich and by Swiss National Science Foundation (200020_182668, 250320_163243 and 206021_170729). GAK acknowledges stimulating discussions with C.A. Bruun at the early stages of this project.

References

[1] B.R. Stanmore, J.F. Brilhac, P. Gilot, The oxidation of soot: a review of experiments, mechanisms and models, Carbon 39 (2001) 2247–2268.
[2] G.A. Kelesidis, A. Nagarkar, U. Trivanovic, S.E. Pratsinis, Toward elimination of soot emissions from jet fuel combustion, Environ. Sci. Technol. 57 (2023) 10276–10283.
[3] O. Schmid, T. Stoeger, Surface area is the biologically most effective dose metric for acute nanoparticle toxicity in the lung, J. Aerosol Sci. 99 (2016) 133–143.
[4] C. Marcolli, F. Mahrt, B. Karcher, Soot PCF: pore condensation and freezing framework for soot aggregates, Atmos. Chem. Phys. 21 (2021) 7791–7843.
[5] S. Khodabakhshi, P.F. Fulvio, E. Andreoli, Carbon black reborn: structure and chemistry for renewable energy harnessing, Carbon 162 (2020) 604–649.

[6] B.W. Zhang, D.A. Wang, B. Yu, F. Zhou, W.M. Liu, Candle soot as a supercapacitor electrode material, RSC Adv. 4 (2014) 2586–2589.
[7] G.A. Kelesidis, S.E. Pratsinis, A perspective on gas-phase synthesis of nanomaterials: process design, impact and outlook, Chem. Eng. J. 421 (2021) 129884.
[8] G.A. Kelesidis, D. Neubauer, L.S. Fan, U. Lohmann, S.E. Pratsinis, Enhanced light absorption and radiative forcing by black carbon agglomerates, Environ. Sci. Technol. 56 (2022) 8610–8618.
[9] R.L. Vander Wal, A.J. Tomasek, Soot nanostructure: dependence upon synthesis conditions, Combust. Flame 136 (2004) 129–140.
[10] M. Alfe, B. Apicella, R. Barbella, J.N. Rouzaud, A. Tregrossi, A. Ciajolo, Structure-property relationship in nanostructures of young and mature soot in premixed flames, Proc. Combust. Inst. 32 (2009) 697–704.
[11] M. Singh, A. Gharpure, R.L. Vander Wal, J. Kollar, C.R. Herd, Effect of fuel composition on carbon black formation pathways, Appl. Sci. 12 (2022) 2569.
[12] T. Ishiguro, Y. Takatori, K. Akihama, Microstructure of diesel soot particles probed by electron microscopy: first observation of inner core and outer shell, Combust. Flame 108 (1997) 231–234.
[13] R.H. Hurt, G.P. Crawford, H.S. Shim, Equilibrium nanostructure of primary soot particles, Proc. Combust. Inst. 28 (2000) 2539–2546.
[14] R.L. Vander Wal, A.J. Tomasek, Soot oxidation: dependence upon initial nanostructure, Combust. Flame 134 (2003) 1–9.
[15] H. Ghiassi, P. Toth, I.C. Jaramillo, J.S. Lighty, Soot oxidation-induced fragmentation: Part 1: the relationship between soot nanostructure and oxidation-induced fragmentation, Combust. Flame 163 (2016) 179–187.
[16] Q.H. Chang, R. Gao, M. Gao, G.S. Yu, F.C. Wang, The structural evolution and fragmentation of coal-derived soot and carbon black during high-temperature air oxidation, Combust. Flame 216 (2020) 111–125.
[17] A.W. Kandas, I.G. Senel, Y. Levendis, A.F. Sarofim, Soot surface area evolution during air oxidation as evaluated by small angle X-ray scattering and CO_2 adsorption, Carbon 43 (2005) 241–251.
[18] F. Ehrburgerdolle, M. Holz, J. Lahaye, Use of N_2, Ar and CO_2 adsorption for the determination of microporosity and surface fractal dimension of carbon-blacks and silicas, Pure Appl. Chem. 65 (1993) 2223–2230.
[19] G.A. Kelesidis, N. Rossi, S.E. Pratsinis, Porosity and crystallinity dynamics of carbon black during internal and surface oxidation, Carbon 197 (2022) 334–340.
[20] T. Ishiguro, N. Suzuki, Y. Fujitani, H. Morimoto, Microstructural changes of diesel soot during oxidation, Combust. Flame 85 (1991) 1–6.
[21] Orion Engineered Carbon, Specialty Carbon Blacks, 2019. https://www.orioncarbons.com/en/oec_3065_r7_carbon_black_pigments_tech_data_v2_5_10_19.pdf.
[22] P. Gilot, F. Bonnefoy, F. Marcuccilli, G. Prado, Determination of kinetic data for soot oxidation - modeling of competition between oxygen diffusion and reaction during thermogravimetric analysis, Combust. Flame 95 (1993) 87–100.
[23] G.A. Kelesidis, S.E. Pratsinis, Estimating the internal and surface oxidation of soot agglomerates, Combust. Flame 209 (2019) 493–499.
[24] J.H. Song, M. Alam, A.L. Boehman, U. Kim, Examination of the oxidation behavior of biodiesel soot, Combust. Flame 146 (2006) 589–604.
[25] M.E. Mueller, G. Blanquart, H. Pitsch, Hybrid Method of Moments for modeling soot formation and growth, Combust. Flame 156 (2009) 1143–1155.
[26] D.P. Chen, Z. Zainuddin, E. Yapp, J. Akroyd, S. Mosbach, M. Kraft, A fully coupled simulation of PAH and soot growth with a population balance model, Proc. Combust. Inst. 34 (2013) 1827–1835.
[27] M.R. Kholghy, G.A. Kelesidis, Surface growth, coagulation and oxidation of soot by a monodisperse population balance model, Combust. Flame 227 (2021) 456–463.
[28] E.L. Cussler, Diffusion: Mass Transfer in Fluid Systems, Cambridge university press, 2009.
[29] M. Sirignano, J. Kent, A. D'Anna, Modeling Formation and oxidation of soot in nonpremixed flames, Energy Fuels 27 (2013) 2303–2315.
[30] J.Q. Camacho, Y.J. Tao, H. Wang, Kinetics of nascent soot oxidation by molecular oxygen in a flow reactor, Proc. Combust. Inst. 35 (2015) 1887–1894.
[31] X. Ma, C.D. Zangmeister, M.R. Zachariah, Soot oxidation kinetics: a comparison study of two tandem ion-mobility methods, J. Phys. Chem. C 117 (2013) 10723–10729.
[32] K.K. Mohanty, J.M. Ottino, H.T. Davis, Reaction and transport in disordered composite media - introduction of percolation concepts, Chem. Eng. Sci. 37 (1982) 905–924.
[33] M. Sahimi, T.T. Tsotsis, Statistical modeling of gas solid reaction with pore volume growth - kinetic regime, Chem. Eng. Sci. 43 (1988) 113–121.
[34] P. Salatino, L. Massimilla, Pressure-drop in flow of a nearly critical fluid through packed-beds of spheres, Chem. Eng. Commun. 93 (1990) 101–109.
[35] R. Jovanovic, E. Marek, S. Maletic, D. Cvetinovic, Z. Markovic, Lattice Monte Carlo simulation of single coal char particle combustion under oxy-fuel conditions, Fuel 151 (2015) 172–181.
[36] A.Y. Zhang, X.W. Liu, Y.S. Xu, T.P. Zhang, M.H. Xu, An improved model of fine particulate matter formation coupling the mechanism of mineral coalescence and char fragmentation during pulverized coal combustion, Proc. Combust. Inst. 39 (2023) 3539–3549.
[37] R. Jovanovic, E.J. Marek, Percolation theory applied in modelling of Fe_2O_3 reduction during chemical looping combustion, Chem. Eng. J. 406 (2021) 126845.
[38] S.J. Lin, L. Ding, Z.J. Zhou, G.S. Yu, Discrete model for simulation of char particle gasification with structure evolution, Fuel 186 (2016) 656–664.
[39] T.S. Totton, D. Chakrabarti, A.J. Misquitta, M. Sander, D.J. Wales, M. Kraft, Modelling the internal structure of nascent soot particles, Combust. Flame 157 (2010) 909–914.
[40] T. Vicsek, F. Family, P. Meakin, Multifractal geometry of diffusion-limited aggregates, Europhys. Lett. 12 (1990) 217–222.
[41] S.K. Friedlander, Smoke, Dust, and Haze: Fundamentals of Aerosol Dynamics, second ed., Oxford University Press, New York, 2000.
[42] P. Meakin, Formation of fractal clusters and networks by irreversible diffusion-limited aggregation, Phys. Rev. Lett. 51 (1983) 1119–1122.
[43] D. Stauffer, A. Aharony, Introduction to Percolation Theory, second ed., Taylor & Francis, 2018.
[44] M.L. Eggersdorfer, S.E. Pratsinis, The structure of agglomerates consisting of polydisperse particles, Aerosol. Sci. Technol. 46 (2012) 347–353.
[45] S. Tolman, P. Meakin, 2, 3 and 4-dimensional diffusion-limited aggregation models, Physica A 158 (1989) 801–816.
[46] E. Stoll, M. Kolb, E. Courtens, Numerical verification of scaling for scattering from fractons, Phys. Rev. Lett. 68 (1992) 2472–2475.
[47] A.D. Sediako, C. Soong, J.Y. Howe, M.R. Kholghy, M.J. Thomson, Real-time observation of soot aggregate oxidation in an environmental transmission electron microscope, Proc. Combust. Inst. 36 (2017) 841–851.
[48] A. Naseri, A.D. Sediako, F. Liu, M. Barati, R.D. Baker, M.J. Thomson, In-situ studies of O_2 and O radical oxidation of carbon black using thermogravimetric analysis and environmental transmission electron microscopy, Carbon 156 (2020) 299–308.
[49] M.L. Botero, Y. Sheng, J. Akroyd, J. Martin, J.A.H. Dreyer, W.M. Yang, M. Kraft, Internal structure of soot particles in a diffusion flame, Carbon 141 (2019) 635–642.
[50] J. Nagle, R.F. Strickland-Constable, Oxidation of carbon between 1000–2000°C, in: Proceedings of the Fifth Conference on Carbon, fifth ed.), 1, Pergamon Press, Oxford, U.K., 1961, pp. 154–164.
[51] K. Al-Qurashi, A.L. Boehman, Impact of exhaust gas recirculation (EGR) on the oxidative reactivity of diesel engine soot, Combust. Flame 155 (2008) 675–695.
[52] Y.Y. Ying, D. Liu, Effects of flame configuration and soot aging on soot nanostructure and reactivity in butanol-doped ethylene diffusion flames, Energy Fuels 32 (2018) 607–624.
[53] K.O. Johansson, F. El Gabaly, P.E. Schrader, M.F. Campbell, H.A. Michelsen, Evolution of maturity levels of the particle surface and bulk during soot growth and oxidation in a flame, Aerosol. Sci. Technol. 51 (2017) 1333–1344.
[54] M. Matsumoto, T. Nishimura, Mersenne Twister: a 623-dimensionally equidistributed uniform pseudorandom number generator, ACM Trans. Model Comput. Simulat 8 (1998) 3–30.
[55] R.L. Vander Wal, A. Yezerets, N.W. Currier, D.H. Kim, C.M. Wang, HRTEM Study of diesel soot collected from diesel particulate filters, Carbon 45 (2007) 70–77.